Supporting information

Triphenylacrylonitrile phenanthroimidazole cored butterfly shaped AIE chromophore for blue and HLCT sensitized fluorescent OLEDs

Jayaraman Jayabharathi*, Shanmugam Thilagavathy, Venugopal Thanikachalam, Jagathratchagan Anudeebhana

Department of Chemistry, Annamalai University, Annamalai nagar, Tamilnadu- 608 002, India

* Address for correspondence

Dr. J. Jayabharathi
Professor of Chemistry
Department of Chemistry
Annamalai University
Annamalai nagar 608 002
Tamilnadu, India.
Tel: +91 9443940735
E-mail: jtchalam2005@yahoo.co.in

Contents

SI-I. (i) General Information and measurements

All the reagents and solvents were purchased from commercial sources and used as received. The emitters were subjected to sublimation to enhance the purity before photoluminescence and electroluminescence investigations. ^{1}H and ^{13}C NMR spectra were recorded at room temperature on Bruker 400 spectrometer in CD_2Cl_2. The mass spectra were recorded on Agilent LCMS VL SD. The UV-Vis spectra were recorded on Lambda 35 PerkinElmer (solution)/ Lambda 35 spectrophotometer (RSA-PE-20) (film). The emission spectra were recorded with Perkin Elmer LS55 spectrometer and quantum yield was measured with fluorescence spectrometer (Model-F7100 with integrating sphere). The decomposition temperature (T_d) and glass transition temperature (T_g) were measured with NETZSCH (DSC-204) (10° C min^{-1}; N_2 atmosphere), respectively. Fluorescence lifetime was estimated by time correlated single-photon counting (TCSPC) method on Horiba Fluorocube-01-NL lifetime system: nano LED is an excitation source with TBX-PS is detector; DAS6 software was employed to analyse the decay by reconvolution method. The absolute quantum yield (PLQY) was determined with fluorescence spectrometer Model-F7100. The quantum yield (ϕ) was measured in dichloromethane with 0.5 M H_2SO_4 solution of quinine (0.54) as reference and calculated using the following equation: $\phi_{unk} = \phi_{std}\left(\frac{I_{unk}}{I_{std}}\right)\left(\frac{A_{std}}{A_{unk}}\right)\left(\frac{\eta_{unk}}{\eta_{std}}\right)^2$, where ϕ_{unk} and ϕ_{std} are the quantum yield of the sample and standard respectively. I_{unk} and I_{std} are the integrated emission intensities of the sample and standard, respectively. η_{unk} and η_{std} are the refractive indices of the sample and standard solution and A_{unk} and A_{std} are the absorbance of the sample and standard, respectively. The quantum yield of thin materials in film has been measured on quartz plate using an integrating sphere [1]. The cyclic voltammetry measurement was carried out in deoxygenated dichloromethane (DCM) with 0.1 M tetrabutylammonium hexafluorophosphate (TBAP) as supporting electrolyte in a three electrode system using BioLogic SP200

potentiostat (BioLogic, France) at room temperature using platinum wire as auxiliary electrode, glass carbon disk as working electrode and Ag/Ag^+ as reference electrode standardized by the redox couple ferrocenium/ferrocene. All solutions were purged with a nitrogen stream for 10 min. before measurement. The procedure was performed at room temperature, and a nitrogen atmosphere was maintained over the solution during measurements. All density functional theory (DFT) calculations were carried out using Gaussian 09 package [2] and Multiwfn [2]. The ground-state (S_0) geometries in the gas phase were initially optimized at the level of B3LYP/6-31G (d, p), a commonly used level for the precise geometry optimization. Then, geometry optimization and excited-state properties based on S_1 geometries were studied using time-dependent DFT (TD-DFT) at the same level. The natural transition orbitals (HONTOs and LUNTOs) with hole-particle contribution, transition density matrix and overlap integral have been studied in detail [3-5].

(ii) OLEDs fabrication and measurement

ITO glass (resistance 20 Ω/sq) were cleaned with acetone, deionized water and isopropanol and dried (120 ^oC) followed by UV-zone treatment (20 min) and transferred into deposition system. The devices were fabricated by multiple source beam deposition method (vacuum pressure - 4×10^{-5} mbar). Evaporation rate of 2-4 Å s^{-1} (organic materials) and 0.1 and 4 $Ås^{-1}$ for LiF and metal electrodes were applied, respectively. The thickness of each decomposition layer was monitored with quartz crystal thickness monitor. The EL measurement was recorded with USB-650-VIS-NIR spectrometer (Ocean Optics, Inc, USA). The current density-voltage-luminance (J-V-L) characteristics were performed using source meter (Keithley 2450) equipped with LS-110 light intensity meter. The external quantum efficiency was determined from luminance, current density and EL spectrum assuming Lambertian distribution.

SI-II. Experimental Section

Materials

The chemicals used in the experimental section were obtained from Sigma-Aldrich. Synthetic route of the emissive materials were outlined in Scheme S1.

Scheme S1. Synthetic route for blue emitters.

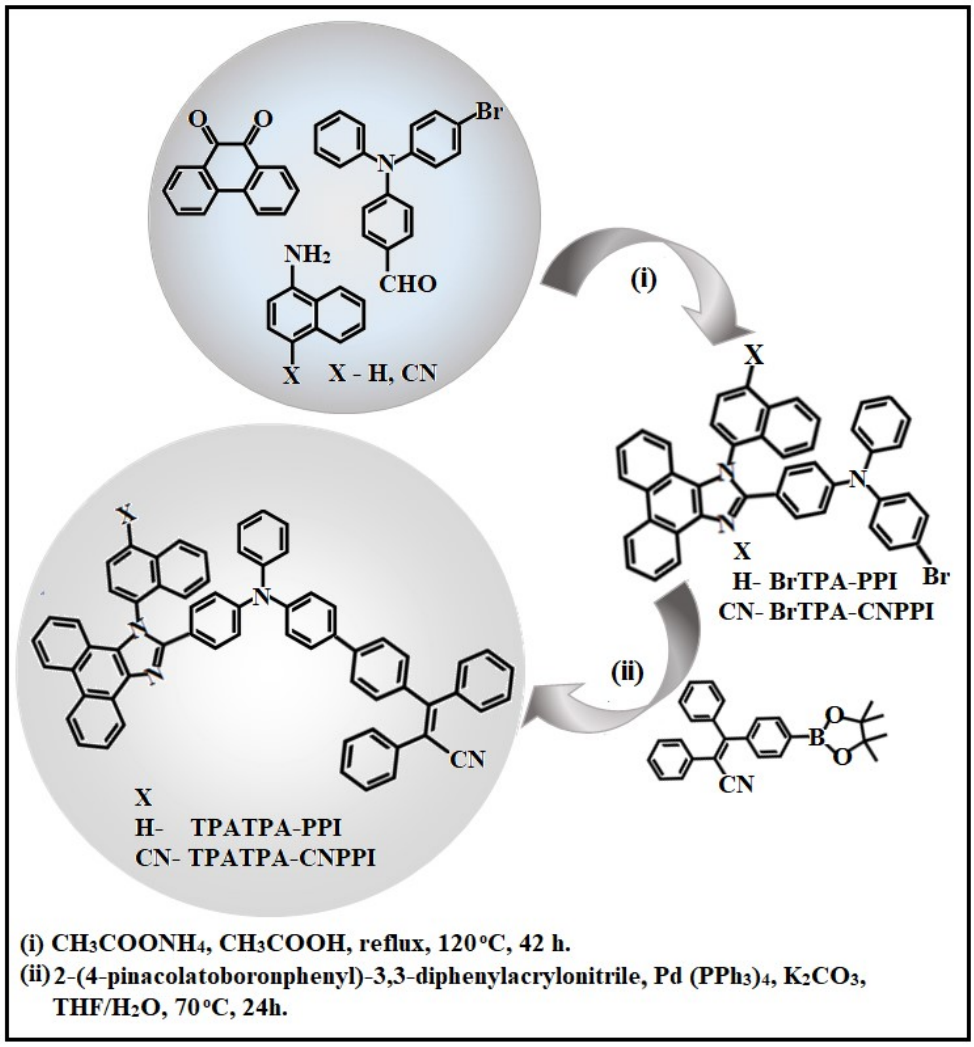

Plate S1. ^{1}H NMR spectrum of N-(4-(1-(naphthalen-1-yl)-1H-phenanthro[9,10-d]imidazol-2-yl)phenyl)-N-phenyl-4'-(1,2,2-diphenylvinylacrylonitrile)-[1,1'-biphenyl]-4-amine (TPATPA-PPI).

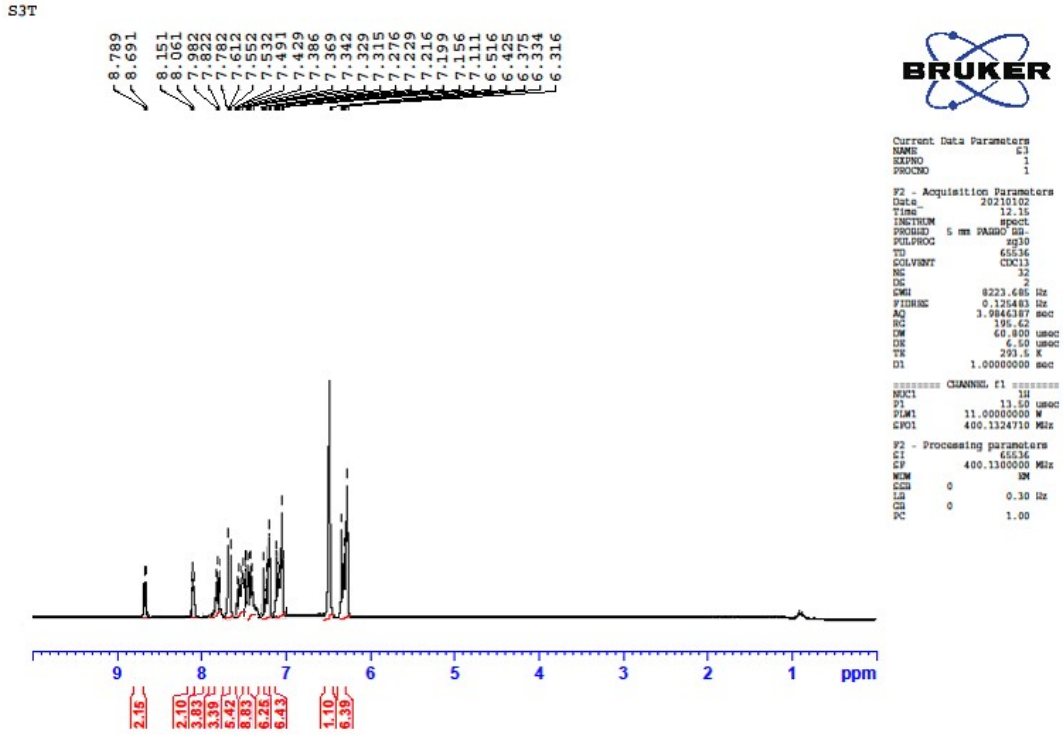

Plate S2. ^{1}H NMR spectrum of 4-(2-(4-(phenyl(4'-(1,2,2-diphenylvinylacrylonitrile)-[1,1'-biphenyl]-4-yl)amino)phenyl)-1H-phenanthro[9,10-d]imidazol-1-yl)-1-naphthonitrile (TPATPA-CNPPI)

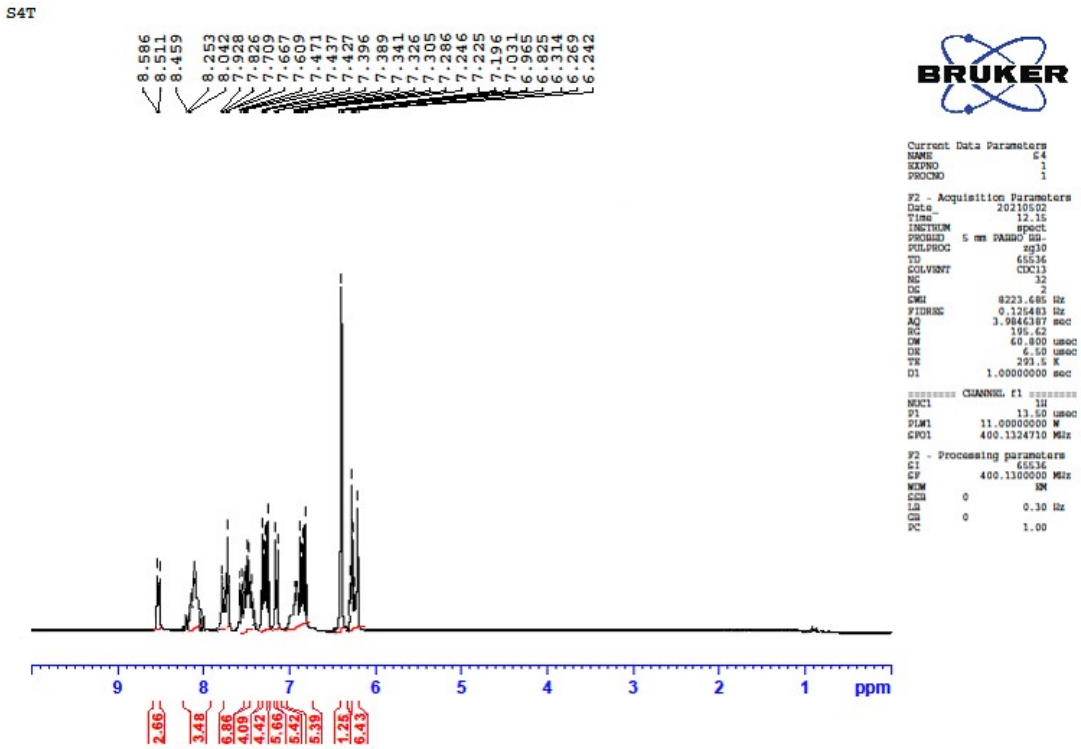

Synthesis

(a) 4-bromo-N-(4-(1-(naphthalen-1-yl)-1H-phenanthro[9,10-d]imidazol-2-yl)phenyl)-N-phenylaniline (BrTPA-PPI)

A mixture of 9,10-phenanthrenequinone (2.54 mmol), 4-(N-(4-bromophenyl)-N-phenylamino) benzaldehyde (2.80 mmol), ammonium acetate (25.4 mmol) and naphthalen-1-amine (3.04 mmol) in acetic acid (10 mL) was refluxed with stirring for 42 h (120°C; N_2**)**. The resulting solid was filtered, washed and dried. Yield: 70%. ^{1}H NMR (400 MHz; $CDCl_3$; δ, ppm): 6.15 (d, 2H), 6.23-6.49 (m, 4H), 6.52 (s, 1H), 6.87 (d, 2H), 6.91-7.10 (m, 4H), 7.18-7.27 (m, 4H), 7.30-7.68 (d, 3H), 7.72-7.80 (m, 4H), 8.12-8.22 (m, 4H). ^{13}C NMR (100 MHz; $CDCl_3$; δ, ppm): 107.0, 112.6, 120.0, 123.0, 124.4, 125.8, 126.0, 127.7, 129.2, 132.0, 133.7, 141.4, 144.8. MS: m/z. 666.61 [M+]; Calcd. 663.91.

(b) 4-(2-(4-((4-bromophenyl)(phenyl)amino)phenyl)-1H-phenanthro[9,10-d]imidazol-1-yl)-1-naphthonitrile (BrTPA-CNPPI)

A mixture of 9,10-phenanthrenequinone (2.54 mmol), 4-(N-(4-bromophenyl)-N-phenylamino) benzaldehyde (2.80 mmol), ammonium acetate (25.4 mmol) and 4-aminonaphthalen-1-carbonitrile (4.32 mmol) in acetic acid (10 mL) was refluxed with continuous stirring for 42 h (120 °C; N_2). The resulting solid was filtered and dried. Yield: 68%. ^{1}H NMR (400 MHz; $CDCl_3$; δ, ppm): 6.21 (d, 2H), 6.35-6.49 (m, 4H), 6.59 (s, 1H), 7.04 (d, 2H), 7.10-7.18 (m, 4H), 7.32 (s, 1H), 7.51-7.64 (d, 2H), 7.69-7.80 (d, 2H), 7.81-7.95 (m, 4H), 8.30 (d, 3H), 8.89 (d, 2H). ^{13}C NMR (100 MHz; $CDCl_3$; δ, ppm): 101.7, 104.3, 111.2, 116.2, 117.4, 119.1, 120.0, 121.3, 124.1, 125.1, 126.0, 130.2, 132.7, 137.8, 139.8, 141.3. MS: m/z. 691.62 [M+]; Calcd. 690.81.

(c) N-(4-(1-(naphthalen-1-yl)-1H-phenanthro[9,10-d]imidazol-2-yl)phenyl)-N-phenyl-4'-(1,2,2-diphenylvinylacrylonitrile)-[1,1'-biphenyl]-4-amine (TPATPA-PPI)

A mixture of $Pd(PPh_3)_4$ (0.04 mmol), BrTPA-PPI (0.4 mmol), 4-(1,2,2-triphenylvinyl)phenylboronic acid pinacol ester (0.52 mmol) and K_2CO_3 (2.0 mmol) in a mixture of ethanol (8.0 mL), toluene (24.0 mL) and H_2O (4.0 mL) was refluxed (70°C; N_2; 24h). The crude was purified by column chromatography. Yield: 65%. ^{1}H NMR (400 MHz, $CDCl_3$, δ, ppm): 6.31-6.42 (m, 6H), 6.51 (s, 1H), 7.11-7.19 (m, 6H), 7.21-7.31 (m, 6H), 7.32-7.42 (m, 8H), 7.49-7.55 (m, 5H), 7.61-7.78 (d, 3H), 7.82-7.98 (m, 3H), 8.10 (d, 2H), 8.73 (d, 2H). ^{13}C NMR (100 MHz, $CDCl_3$, δ, ppm): 107.9, 109.7, 113.8, 120.4, 122.4, 124.1, 126.1, 126.4, 127.7, 128.0, 129.4, 129.9, 130.9, 132.9, 134.5, 135.6, 137.9, 139.5, 140.1, 147.4. MS: m/z. 867.05 [M^+]; Calcd. 866.71. Anal. Cacld (%) for $C_{64}H_{42}N_4$: C, 88.66; H, 4.88; N, 6.46. Found: C, 88.42; H, 4.80; N, 6.40.

(d) 4-(2-(4-(phenyl(4'-(1,2,2-diphenylvinylacrylonitrile)-[1,1'-biphenyl]-4-yl)amino) phenyl)-1H-phenanthro[9,10-d]imidazol-1-yl)-1-naphthonitrile (TPATPA-CNPPI)

A mixture of $Pd(PPh_3)_4$ (0.04 mmol), BrTPA-CNPPI (0.4 mmol), 4-(1,2,2-triphenylvinyl)phenylboronic acid pinacol ester (0.52 mmol) and K_2CO_3 (2.0 mmol) in a mixture of ethanol (8.0 mL), toluene (24.0 mL) and H_2O (4.0 mL) was refluxed (70 °C; N_2; 24h). The crude was purified by column chromatography. Yield: 60%. ^{1}H NMR (400 MHz; $CDCl_3$; δ, ppm): 6.24 (m, 6H), 6.31 (s, 1H), 6.82-7.19 (m, 5H), 7.22-7.30 (m, 5H), 7.32-7.38 (m, 5H), 7.39-7.42 (m, 4H), 7.43-7.60 (m, 4H), 7.66-7.92 (m, 6H), 8.04-8.45 (m, 3H), 8.51-8.58 (d, 2H). ^{13}C NMR (100 MHz; $CDCl_3$; δ, ppm): 105.7, 107.5, 111.8, 119.7, 120.2, 123.8, 125.1, 126.8, 127.9, 128.5, 128.8, 129.5, 130.9, 131.5, 134.7, 137.8, 139.9, 140.9, 143.0, 145.6. MS: m/z. 892.05 [M^+]; Calcd. 891.74. Anal. Cacld (%) for $C_{65}H_{41}N_5$: C, 87.52; H, 4.63; N, 7.85. Found: C, 87.42; H, 4.57; N, 7.79.

SI-III. Charge-Transfer Indexes

The hole-particle pair interactions have been related to the distance covered during the excitations: one possible descriptor Δr index could be used to calculate the average distance which is weighted in function of the excitation coefficients.

$$\Delta r = \frac{\Sigma_{ia} k_{ia}^2 \left| \langle \varphi_a | r | \varphi_a \rangle - \langle \varphi_i | r | \varphi_i \rangle \right|}{\Sigma_{ia} K_{ia}^2} \quad \text{…….. (S1)}$$

where $\left| \langle \varphi_i | r | \varphi_i \rangle \right|$ is the norm of the orbital centroid [6–9]. Δr index will be expressed in Å. The density variation associated to the electronic transition is given by

$$\Delta\rho(r) = \rho_{EX}(r) - \rho_{GS}(r) \quad \text{..... (S2)}$$

where $\rho_{GS}(r)$ and $\rho_{EX}(r)$ are the electron densities of the ground and excited states, respectively. Two functions, $\rho_+(r)$ and $\rho_-(r)$ corresponds to the points in space where an increment or a depletion of the density upon absorption is produced and they can be defined as follows:

$$\rho_+(r) = \begin{Bmatrix} \Delta\rho(r) if \Delta\rho(r) > 0 \\ 0 \quad if \Delta\rho(r) < 0 \end{Bmatrix} \quad \text{..... (S3)}$$

$$\rho_-(r) = \begin{Bmatrix} \Delta\rho(r) if \Delta\rho(r) < 0 \\ 0 \quad if \Delta\rho(r) > 0 \end{Bmatrix} \quad \text{..... (S4)}$$

The barycenters of the spatial regions R_+ and R_- are related with $\rho_+(r)$ and $\rho_-(r)$ and are shown as,

$$R_+ = \frac{\int r\rho_+(r)dr}{\int \rho_+(r)dr} = (x_+, y_+, z_+) \quad \text{..... (S5)}$$

$$R_- = \frac{\int r\rho_-(r)dr}{\int \rho_-(r)dr} = (x_-, y_-, z_-) \quad \text{..... (S6)}$$

The spatial distance (D_{CT}) between the two barycenters (R_+ and R_-) electron density distributions can be used to measure the CT excitation length

$$D_{CT} = \left| R_+ - R_- \right| \quad \text{(S7)}$$

The transferred charge (q_{CT}) can be obtained by integrating over all space $\rho_+(\rho_-)$. Variation in dipole moment between the ground and the excited states (μ_{CT}) can be computed by the following relation:

$$\|\mu_{CT}\| = D_{CT}\int \rho_+(r)dr = D_{CT}\int \rho_-(r)dr \quad \text{(S8)}$$

$$= D_{CT}q_{CT} \quad \text{(S9)}$$

The difference between the dipole moment $\|\mu_{CT}\|$ have been computed for the ground and excited states ($\Delta\mu_{ES-GS}$). The two centroids of charges (C^+/C^-) associated to the positive and negative density regions are calculated as follows. First the root-mean-square deviations along the three axis (σ_{aj}, j = x, y, z; a = + or –) are computed as,

$$\sigma_{a,j} = \sqrt{\frac{\sum_i \rho_a(r_i)(j_i - j_a)^2}{\sum_i \rho_a(r_i)}} \quad \text{(S10)}$$

The two centroids (C_+ and C_-) are defined as

$$C_+(r) = A_+ e\left(-\frac{(x - x_+)^2}{2\sigma_{+x}^2} - \frac{(y - y_+)^2}{2\sigma_{+y}^2} - \frac{(z - z_+)^2}{2\sigma_{+z}^2}\right) \quad \text{(S11)}$$

$$C_-{}_+(r) = A_- e\left(-\frac{(x - x_-)^2}{2\sigma_{-x}^2} - \frac{(y - y_-)^2}{2\sigma_{-y}^2} - \frac{(z - z_-)^2}{2\sigma_{-z}^2}\right) \quad \text{(S12)}$$

The normalization factors (A+ and A_) are used to impose the integrated charge on the centroid to be equal to the corresponding density change integrated in the whole space:

$$A_{+} = \frac{\int \rho_{+}(r)dr}{\int e\left(-\frac{(x-x_{-})^2}{2\sigma_{+x}^2} - \frac{(y-y_{-})^2}{2\sigma_{+y}^2} - \frac{(z-z_{-})^2}{2\sigma_{+z}^2}\right)dr} \quad \text{..... (S13)}$$

$$A_{-} = \frac{\int \rho_{-}(r)dr}{\int e\left(-\frac{(x-x_{-})^2}{2\sigma_{-x}^2} - \frac{(y-y_{-})^2}{2\sigma_{-y}^2} - \frac{(z-z_{-})^2}{2\sigma_{-z}^2}\right)dr} \quad \text{..... (S14)}$$

H index is defined as half of the sum of the centroids axis along the D–A direction, if the D–A direction is along the X axis, H is defined by the relation:

$$H = \frac{\sigma_{+x} + \sigma_{-x}}{2} \quad \text{..... (S15)}$$

The t index represents the difference between D_{CT} and H:

$$t = D_{CT} - H \quad \text{..... (S16)}$$

Figure S1. Natural transition orbital pairs (HONTOs and LUNTOs) with transition character of TPATPA-PPI [*f*-oscillator strength and %- weights of hole-particle].

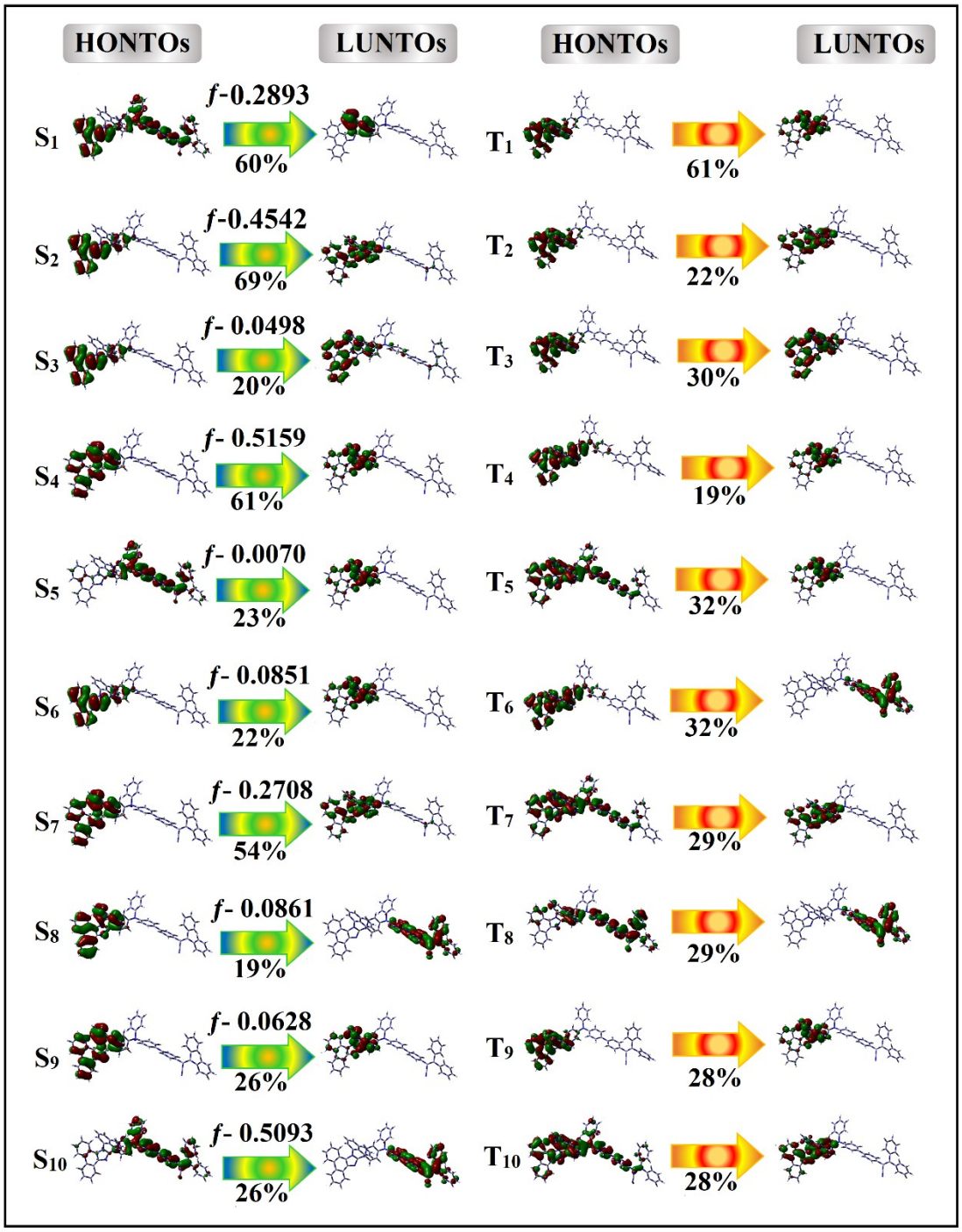

Figure S2. (a) Cyclic voltammogram (100 mV/s) of TPATPA-PPI and TPATPA-CNPPI in dry DCM using 0.1 M TBAP as supporting electrolyte; Normalised absorption spectra of TPATPA-PPI (b) and TPATPA-CNPPI(c) in THF-H_2O with different water fractions and (d) ML and PL spectra.

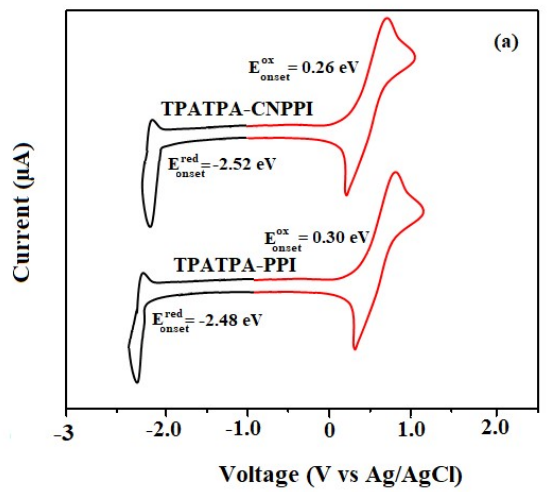
(a)
E^{ox}_{onset} = 0.26 eV
TPATPA-CNPPI
E^{red}_{onset}=-2.52 eV
E^{ox}_{onset} = 0.30 eV
TPATPA-PPI
E^{red}_{onset}= -2.48 eV
Current (μA)
Voltage (V vs Ag/AgCl)

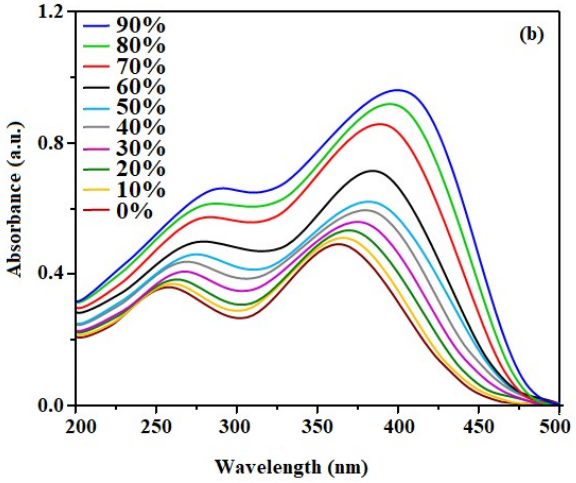
(b)
90%
80%
70%
60%
50%
40%
30%
20%
10%
0%
Absorbance (a.u.)
Wavelength (nm)

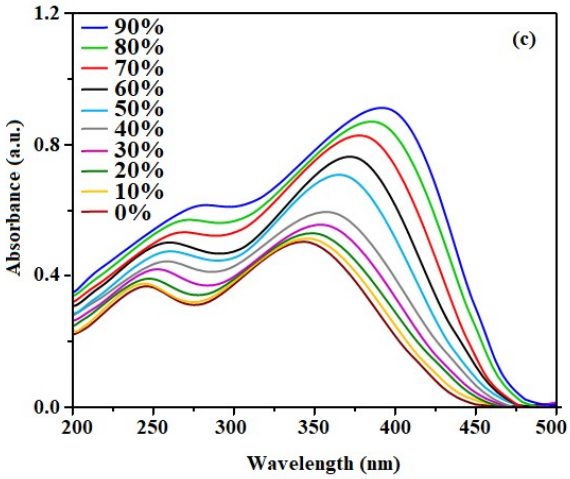
(c)
90%
80%
70%
60%
50%
40%
30%
20%
10%
0%
Absorbance (a.u.)
Wavelength (nm)

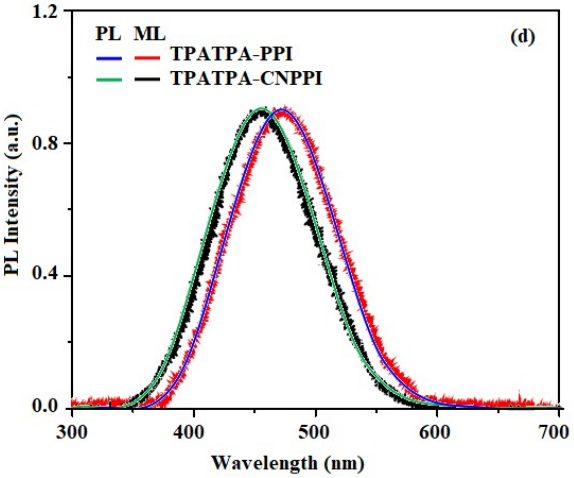
(d)
PL ML
TPATPA-PPI
TPATPA-CNPPI
PL Intensity (a.u.)
Wavelength (nm)

Figure S3. Optimised geomentry, HOMO-LUMO orbitals, net dipole moment of couples and intermolecular interactions of couples I-III of TPATPA-PPI.

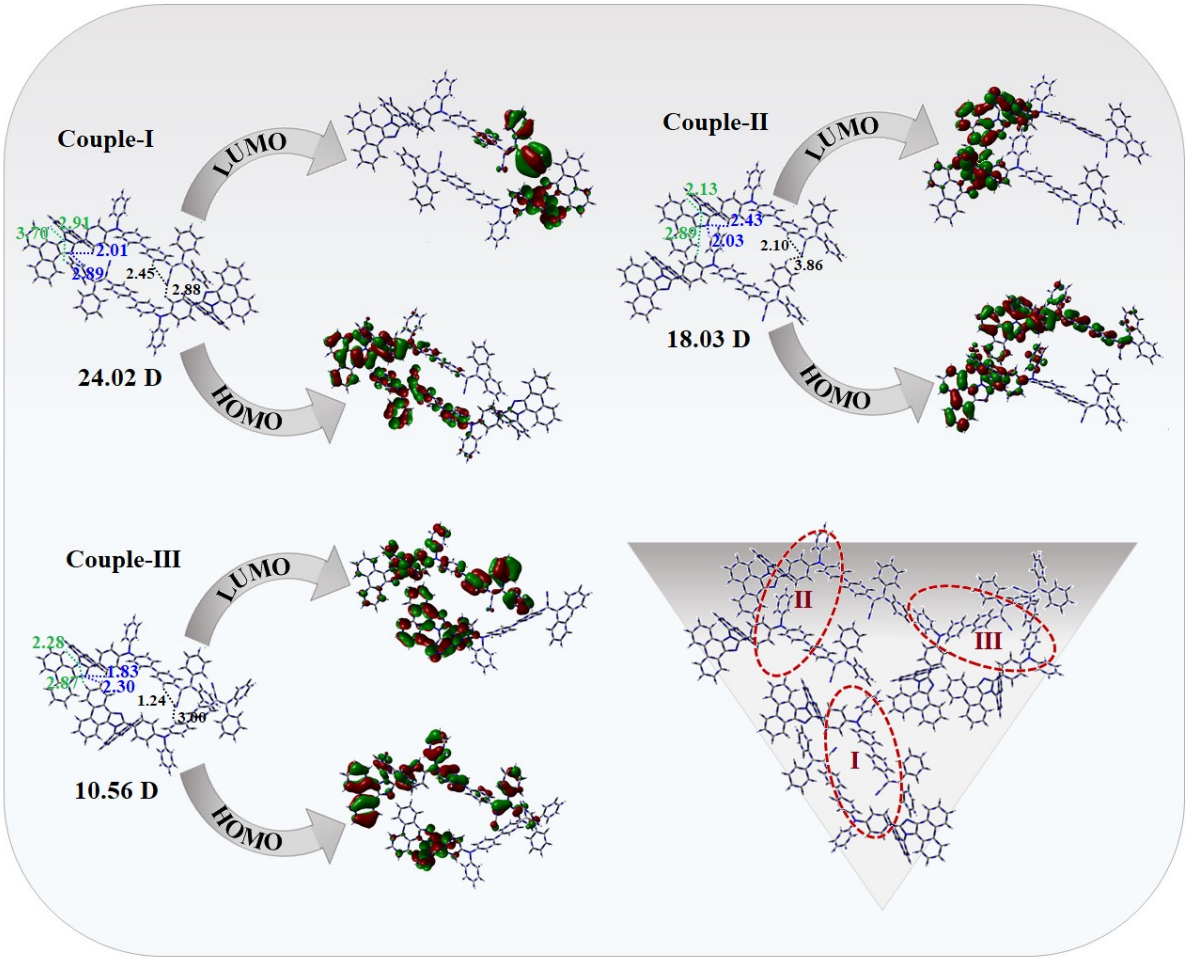

SI-IV. (a) Solvatochromism for HLCT character

The optical characteristics of emissive materials were studied in solution as well as solid by absorption and emission studies. When cyano group is incorporated, the modification in charge-transfer state red-shifted the absorption and emission. The CN group influences the electronic properties as well as band-gap. It is in accordance with quantum chemical calculations. The emission peak was red shifted as increasing the solvent polarity because of polarization induced optical shift (Tables S3 and S4: Figure S4). The PL spectra gradually widened indicates that their excited state have strong CT character when compared to ground state and further stabilized by polar solvents.

Figure S4. Solvatochromism: (a) Normalised absorption spectra and (b) Normalised emission spectra of TPATPA-PPI and TPATPA-CNPPI.

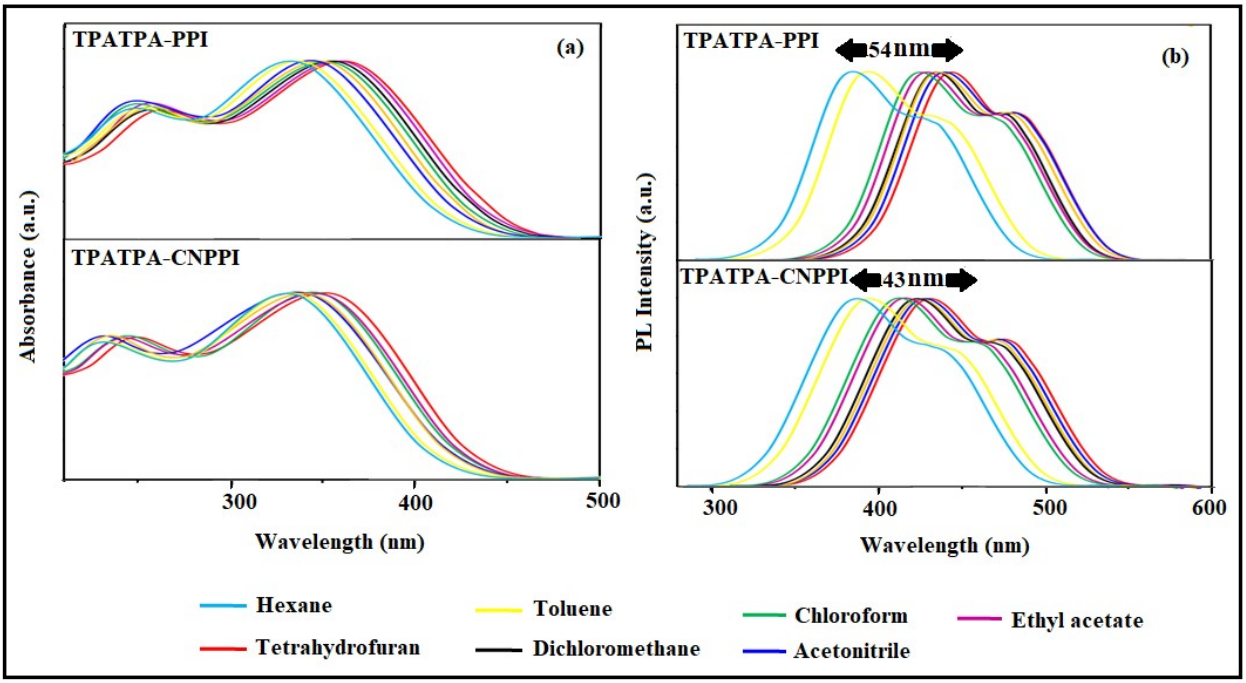

(b) Transition density matrix (TDM) plot

The existence of LE and CT states can be discussed from wave function of electron-hole pairs transition density matrix (TDM) plot. The diagonal region represents LE component and off-diagonal region shows CT component. Upon excitation, electron transferred from donor and localized on acceptor: depending upon intramolecular geometrical and electronic

coupling, transferred electron delocalized from the region of nearby donor to the vicinity of acceptor. This effect can be qualitatively studied by analysing electron density distribution at ground and excited states. Computed electron-hole properties, distance between hole and electron, transition density, H and t indexes and RMSD of electron and hole of these emitters are displayed in Tables S10-S12.

Figure S5. Contour plot of transition density matrices (TDM) with hole and particle distribution [green - increasing electron density and blue- decreasing electron density] of TPATPA-PPI.

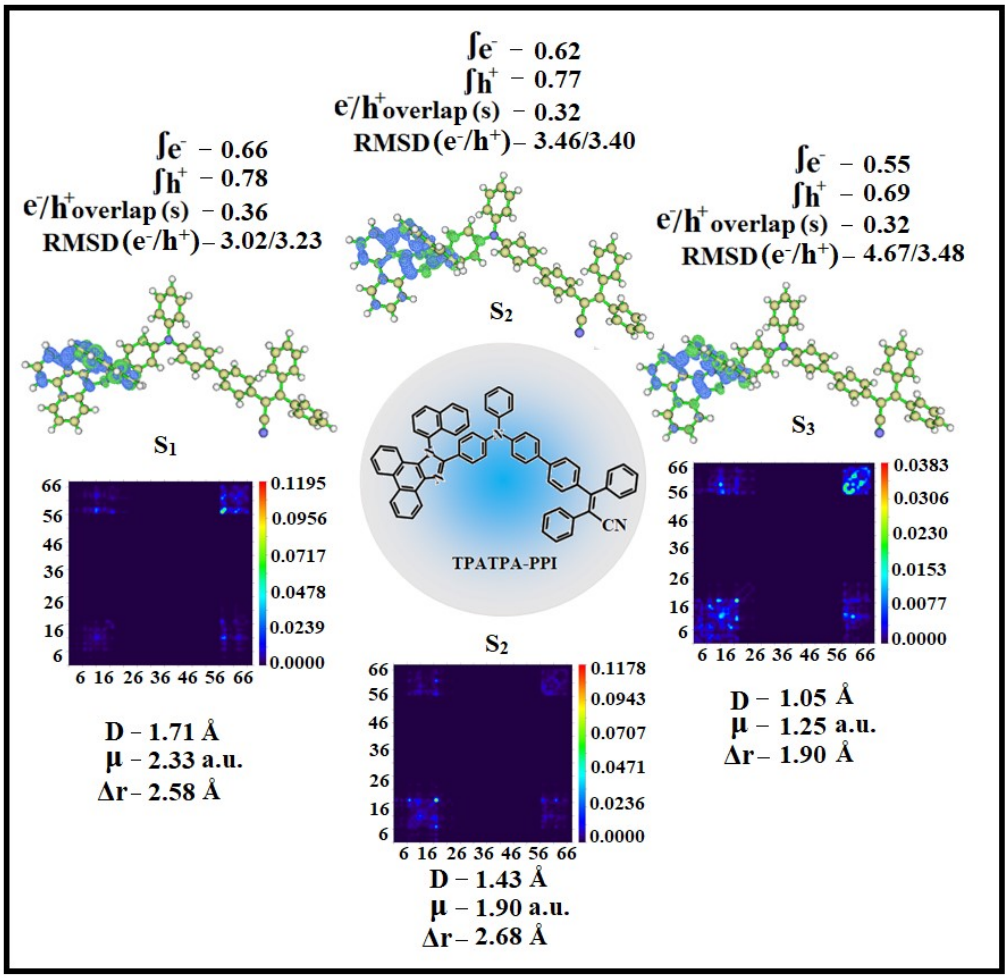

The integral value of hole and electron with transition density have been shown in Tables S5-S9. The integral overlap of hole-electron distribution (S) is a measure of spatial separation of hole and electron. The integral overlap (S) of hole and electron and distance (D) between centroids of hole and electron proved the existence of LE and CT states. These emitters

show small S and high D, indicates higher charge transfer (CT) variation of dipole moment with respect to S_0 state. These values are directly evaluated based on the position of centroid of hole and electron. RMSD of hole or electron characterizes their distribution breadth: RMSD of both electron and hole is higher in X direction indicates electron and hole distribution is much broader in Y and Z directions (Tables S5-S8). The overlap between the region of density depletion and increment have been visualised by using two centroids of charges (equations S9 and S10). The H and t indexes for TPATPA-PPI and TPATPA-CNPPI are tabulated (Tables S7 and S8). The CT index, *i.e.* index difference between D_{CT} and H index is another measure of the separation of hole-electron (equations S15 and S16). The D_{CT} of TPATPA-PPI and TPATPA-CNPPI has been calculated to be 8.585 and 0.296, respectively and the calculated. *H*/*t* indexes are of TPATPA-PPI (6.939/2.111), TPATPA-CNPPI (7.386/7.177) (Figure S7 and Table S9). For TPATPA-PPI and TPATPA-CNPPI, the non-zero *t* is negative in all directions: overlap of hole and electron is very severe and eign value is greater than 0.96, supports the hybridization and described in terms of dominant excitation pair in terms of 94 % of transition.

The hybridization of these materials have been further evidenced by Δr index (Tables S1 and S2). The Δr index (equation S1) is average of hole (h^+)-electron (e^-) distance ($d_{h^+ - e^-}$) upon excitation which indicates the nature of excitation type, LE or CT: valence excitation (LE) is related to short distances ($d_{h^+ - e^-}$) while larger distances ($d_{h^+ - e^-}$) related to CT excitation. The triplet exciton is transformed to singlet exciton *via* RISC process with high energy excited state (hot CT channel) which are beneficial for triplet exciton conversion in electroluminescence process without delayed fluorescence [10, 11]. The CT excitons have been formed with weak binding energy (E_b) on higher excited states [12, 13]. As a result, the exciton utilization can be harvested in TPATPA-PPI and TPATPA-CNPPI like phosphorescent

materials. The hybridization between LE and CT components leads to high EUE and enhanced OLEDs performances (Table 2) [13].

Figure S6. Contour plot of transition density matrices (TDM) with hole and particle distribution [green - increasing electron density and blue- decreasing electron density] of TPATPA-CNPPI.

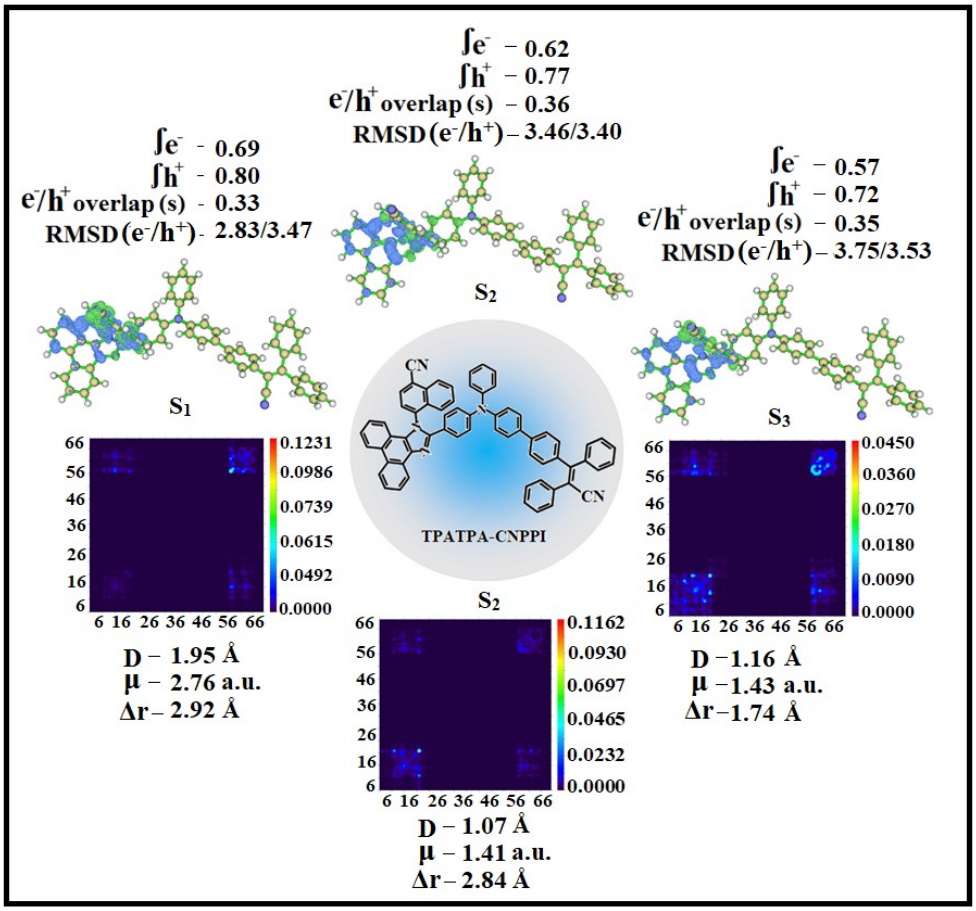

Figure S7. Graphical representation of D_{CT} and centroid of charges [C+(r) / C-(r); isosurface (0.1 a.u)].

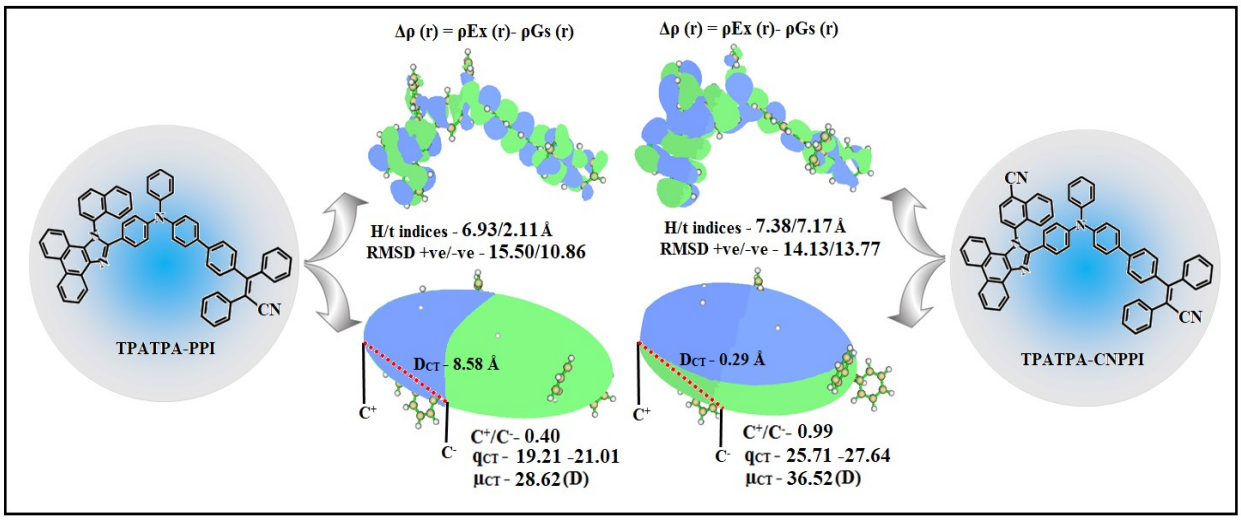
Δρ (r) = ρEx (r)- ρGs (r)
Δρ (r) = ρEx (r)- ρGs (r)
H/t indices - 6.93/2.11 Å
RMSD +ve/-ve - 15.50/10.86
H/t indices - 7.38/7.17 Å
RMSD +ve/-ve - 14.13/13.77
TPATPA-PPI
CN
DCT - 8.58 Å
C+
C-
C+/C- 0.40
qCT - 19.21 -21.01
μCT - 28.62 (D)
DCT - 0.29 Å
C+
C-
C+/C- 0.99
qCT - 25.71 -27.64
μCT - 36.52 (D)
CN
CN
TPATPA-CNPPI

(c) Potential energy scan (PES)

The potential energy surface (PES) scan have been plotted as a function of twist angle between C2 substituent and phenanthroimidazole core in gas phase and different polar solvents (Figures S8). In gas phase, it is impossible for S3 mixing with S1 state as a result of large energy gap between them. An increasing solvent polarity, the large dipole moment of S3 state leads to energetic stabilization. In low polarity solvent (hexane), S3 state can intercross with S1 state whereas in high polarity solvent (acetonitrile), S3 state energy decreases sharply and becomes lowest excited state. In moderate polar solvents (chloroform), the energetic closeness results in an enhanced mixing of S3 with S1. Therefore, S1 state is dominated by LE character in low polar medium; S1 state is dominated by mixing LE and CT character in moderate polar medium and S1 state is dominated by CT character in high polar medium.

Figure S8. Potential energy scan (PES) and different polar solvents of (a) TPATPA-PPI and (b) TPATPA-CNPPI.

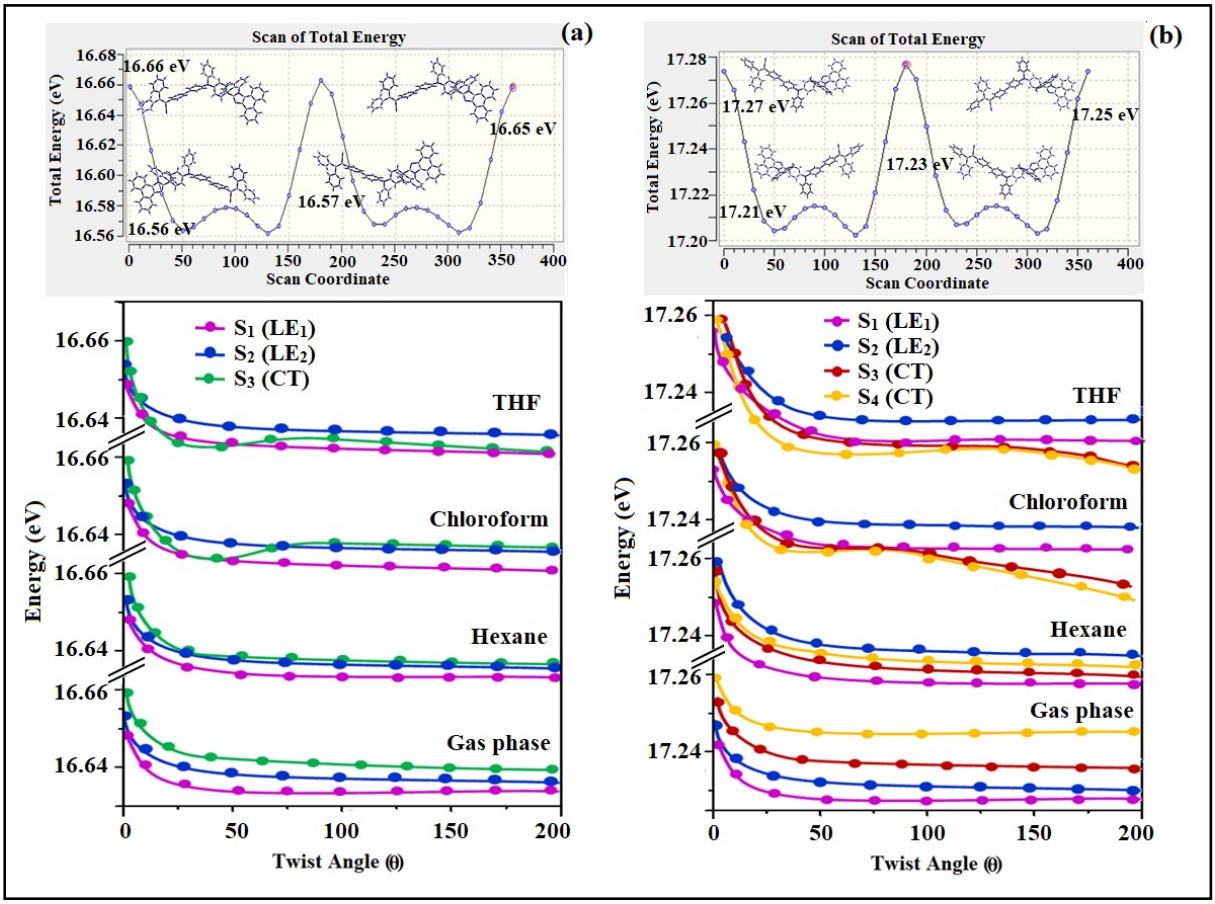

(d) Hot exciton mechanism

The interstate hybridization coupling between LE and CT state wave function are of $\Psi_{S_1/S_2} = c_{LE}.\Psi_{LE} \pm c_{CT}.\Psi_{CT}$. The % CT of these emitters increases as increasing the aromatic fragment size and also partially influenced by steric hindrance. The % LE in S1 state, these emitter's exhibit higher photoluminance efficiency (η_{PL}) and high lying CT state increased the EUE (Figure S9). Therefore, degree of hybridization between LE and CT states depends not only initial E_{LE}-E_{CT} energy gap but also their interstate coupling strength [14]. Especially, the large energy differences of the initial LE and CT states in TPATPA-PPI lead to non-equivalent hybridization between LE and CT states, whereas the isoenergetic LE and CT states of TPATPA-CNPPI belongs to quasi-equivalent hybridization. The vertical excitation energies for the pure LE state were obtained for the corresponding conjugated molecular backbone by replacing the cyano group with hydrogen atoms and the vertical excitation energy of pure CT state were roughly estimated according to the energy conservation ($E_{S1} + E_{S2} = E_{LE} + E_{CT}$).

Figure S9. Reverse intersystem crossing.

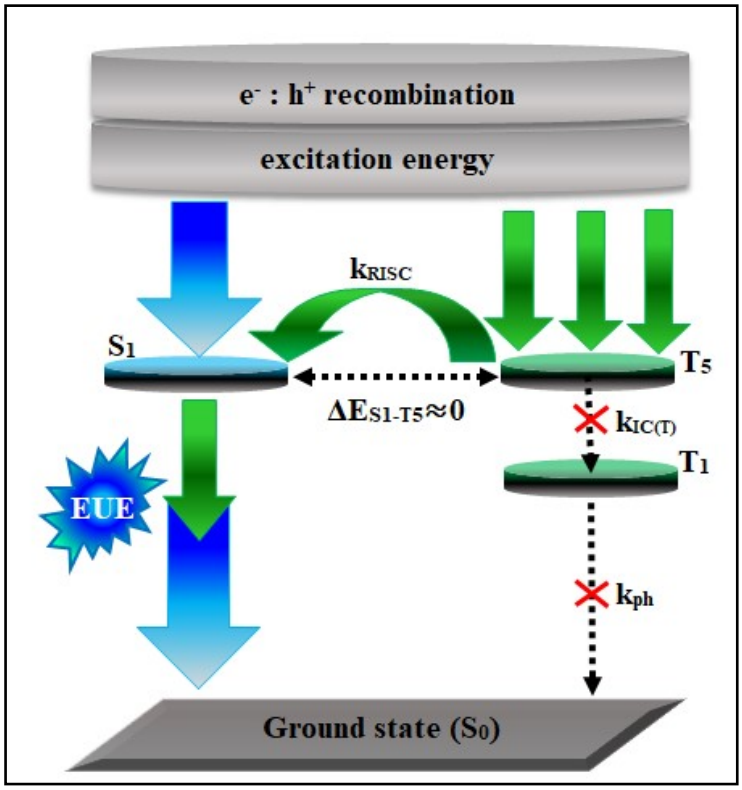

In hot exciton mechanism, the core concept is increasing the rate of h_{RISC} (k_{hRISC}) from Tn (n ≥ 2) to Sm (m ≥ 1), while decreasing the rate of internal conversion (k_{IC}) from Tn (n ≥ 2) to T1. When $k_{hRISC} \gg k_{IC}$, the non-radiative triplet excitons could be fully converted into radiative singlet excitons, resulting in improvement of device efficiency. According to Fermi's golden rule [9], k_{hRISC} depends on ΔE_{ST} and spin-orbit coupling (SOC), as expressed in formula S17

$$k_{hRISC} \propto \left| \frac{\left\langle \Psi_{S_m} \middle| \hat{H}_{SO} \middle| \Psi_{T_n} \right\rangle}{\Delta E_{S_m T_n}} \right|^2 \quad (\mathrm{m} \geq 1, n \geq 2) \text{.....S17}$$

in which Ψ_{T_n} and Ψ_{S_m} represent the wave functions of initial (Tn, n ≥ 2) and final (Sm, m ≥ 1) states of h_{RISC}, respectively, SO is the operator for SOC $\left\langle \Psi_{S_m} \middle| \hat{H}_{SO} \middle| \Psi_{T_n} \right\rangle$ and represent the SOC matrix element and the energy difference between Tn and Sm, $\Delta E_{S_m T_n}$. Therefore, increasing k_{hRISC} from T_n to S_m requires small $\Delta E_{S_m T_n}$ and large SOC. On the other hand, k_{IC} can be expressed by using the following formula S18 [10]

$$k_{IC} \propto \left| \frac{\left\langle \Psi_{T_n} \middle| \hat{T}_N \middle| \Psi_{T_1} \right\rangle}{\Delta E_{T_n T_1}} \right|^2 (n \geq 2) \quad \text{.....S18}$$

where, Ψ_{T_n} and Ψ_{T_1} represent the wave functions of high-lying (Tn, n ≥ 2) and low-lying triplet states of IC process, respectively, Ψ_{T_n} and Ψ_{T_1}, $\Psi_{T_n}\left\langle \hat{T}_N \middle| \Psi_{T_1} \right\rangle \Delta E_{T_n T_1}$ is the electronic operator describing the oupling energy gap between Tn and T1 states. In consequence, decreasing k_{IC} from Tn to T1 requires poor electronic coupling factor and large $\Delta E_{T_n T_1}$. Usually, a large energy gap between the initial and final state plays a critical role in the slow k_{IC}. So, three

positive factors including large $\Delta E_{T_n T_1}$, small $\Delta E_{S_m T_1}$ and large $\langle \Psi_{S_m} | \hat{T}_{S_0} | \Psi_{T_n} \rangle$ are liable to achieve efficient OLEDs with “hot exciton” mechanism.

SI-V. Performances of single carrier devices

Figure S10. (a) Current density-voltage (J-V) characteristics of single carrier devices; (b)Luminescence-current density plot and (c) Schematic representation of HLCT-SF OLEDs.

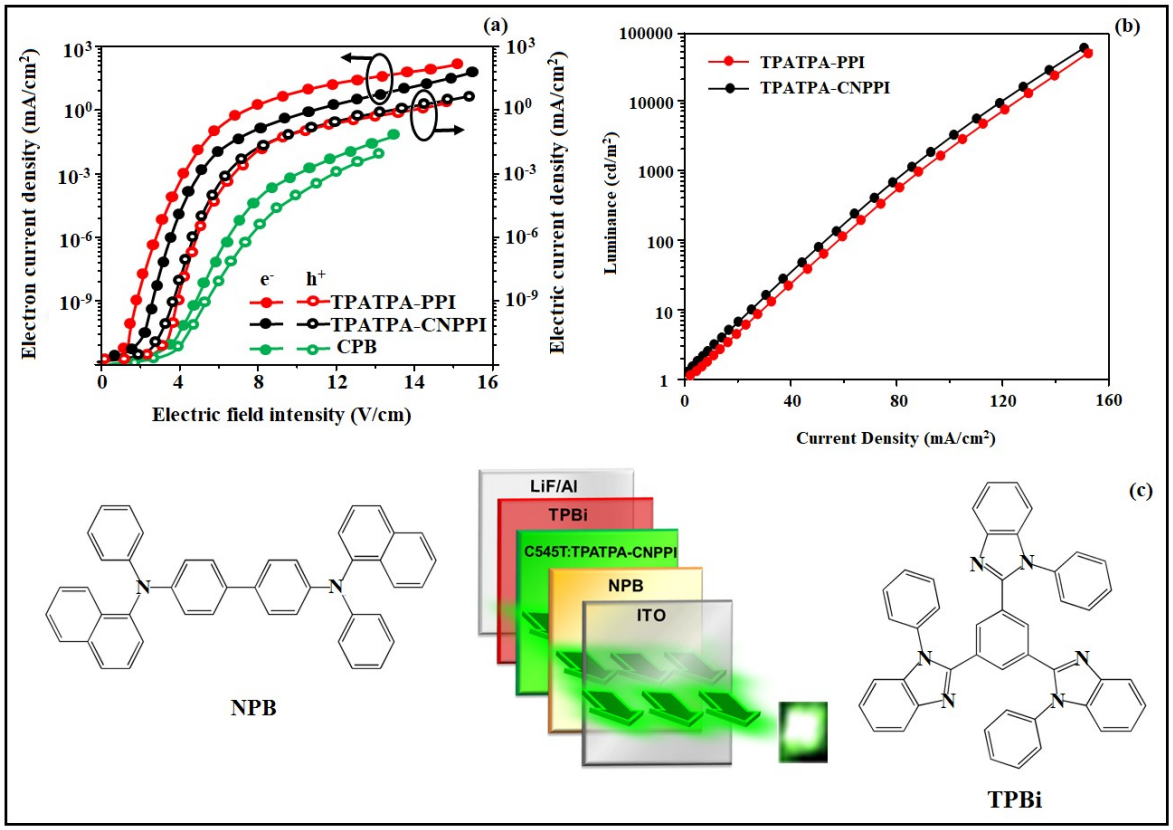

SI-VI. Tables

Table S1. Computed singlet (E_S) and triplet (E_T) energies (eV), oscillator strength (*f*) and dipole moment (μ, D) of TPATPA-PPI from NTOs.

Energy level	E_S	Oscillator strength (f)	Δr index	NTO Transitions	E_T	NTO Transitions	μ (D)
1	3.12	0.6780	2.58	74% 169 → 172	1.45	40% 166 → 170	2.33
2	3.19	0.4330	2.68	44% 166 → 170	1.98	21% 169 → 183	1.90
3	3.30	0.0480	1.90	19% 168 → 170	2.39	28% 165 → 172	1.25
4	3.41	0.0084	2.53	19% 169 → 176	3.01	28% 165 → 172	1.30
5	3.42	0.5333	3.28	54% 168 → 171	3.12	25% 168 → 171	1.86
6	3.51	0.0695	3.41	21% 166 → 170	3.15	25% 168 → 171	1.94
7	3.56	0.2755	2.07	52% 169 → 172	3.19	25% 168 → 171	1.76

				8		1	
8	3.59	0.0582	3.18	$\overset{18\%}{169 \rightarrow 18}$	3.20	$\overset{25\%}{168 \rightarrow 17}$	2.59
				3		1	
9	3.60	0.0594	2.15	$\overset{38\%}{168 \rightarrow 17}$	3.22	$\overset{25\%}{162 \rightarrow 18}$	1.61
				3		1	
10	3.74	0.5152	2.91	$\overset{26\%}{165 \rightarrow 17}$	3.26	$\overset{25\%}{162 \rightarrow 18}$	2.62
				2		1	

Table S2. Computed singlet (E_S) and triplet (E_T) energies (eV), oscillator strength (*f*) and dipole moment (μ, D) of TPATPA-CNPPI from NTOs.

Energy level	E_S	Oscillator strength (f)	Δr index	NTO Transitions	E_T	NTO Transitions	μ (D)
1	3.34	0.2893	2.92	60% 169 → 174	1.13	61% 169 → 174	2.76
2	3.38	0.4542	2.84	69% 173 → 176	1.98	22% 173 → 188	1.41
3	3.41	0.0498	1.74	20% 171 → 176	2.39	30% 170 → 176	1.43
4	3.43	0.5159	3.13	61% 172 → 175	3.01	19% 171 → 183	2.85
5	3.52	0.0070	3.39	23% 173 → 181	3.34	32% 172 → 175	1.24
6	3.55	0.0851	2.36	22% 169 → 177	3.36	32% 172 → 175	1.94
7	3.56	0.2708	2.80	54% 173 → 183	3.39	29% 165 → 174	1.07
8	3.57	0.0861	1.62	19% 172 → 177	3.41	29% 165 → 174	1.15
9	3.59	0.0628	2.94	26% 171 → 176	3.42	28% 166 → 186	2.01
10	3.94	0.5093	1.85	26% 170 → 176	3.43	28% 166 → 186	1.04

Table S3. Photophysical properties of TPATPA-PPI in different solvents.

Solvents	**ε**	**n**	**f (ε,n)**	**λ_{ab} (nm)**	**υ_{ab} (cm^{-1})**	**λ_{flu} (nm)**	**υ_{flu} (cm^{-1})**	**υ_{ss} (cm^{-1})**
Hexane	1.88	1.37	0.0004	336	29762	389	25707	4055
Toluene	2.38	1.49	0.014	337	29674	393	25445	4228
Chloroform	4.81	1.44	0.148	358	27933	429	23310	4623
ethyl acetate	6.09	1.41	0.186	361	27701	437	22883	4818
THF	7.52	1.40	0.209	362	27624	443	22573	5051
DCM	9.08	1.42	0.218	359	27855	442	22624	5231
DMF	36.7	1.42	0.276	353	28329	441	22676	5653
acetonitrile	37.5	1.34	0.305	346	28902	442	22624	6277

Table S4. Photophysical properties of TPATPA-CNPPI in different solvents.

Solvents	**ε**	**n**	**f (ε,n)**	**λ_{ab} (nm)**	**υ_{ab} (cm^{-1})**	**λ_{flu} (nm)**	**υ_{flu} (cm^{-1})**	**υ_{ss} (cm^{-1})**
Hexane	1.88	1.37	0.0004	330	30303	387	25840	4463
Toluene	2.38	1.49	0.014	332	30120	394	25381	4740
Chloroform	4.81	1.44	0.148	346	28901	419	23866	5035
ethyl acetate	6.09	1.41	0.186	346	28902	421	23753	5149
THF	7.52	1.40	0.209	351	28490	430	23256	5234
DCM	9.08	1.42	0.218	346	28901	427	23419	5483
DMF	36.7	1.42	0.276	341	29326	428	23364	5961
acetonitrile	37.5	1.34	0.305	336	29762	429	23310	6452

Table S5. Computed hole and electron overlap (S), distance between centroids of hole and electron (D, Å) and dipole moment (μ) for singlet states of TPATPA-PPI.

State	Hole integral	Electron integral	Integral of transition density	Integral overlap of h^+- e^- (S)	Centroid of hole (Å)			Centroid of electron (Å)			D (Å)	μ (a.u)
					x	y	z	x	y	z		
S1	0.7763	0.6682	0.3663	0.3663	-7.0128	-0.0280	1.1310	-5.6180	0.0655	2.1185	1.71	2.33
S2	0.7753	0.6266	-0.0121	0.3220	-7.3388	-0.5186	0.4509	-5.9812	-0.2725	0.0507	1.43	1.90
S3	0.6965	0.5595	-0.0058	0.3002	-7.0070	-0.4392	0.4716	-6.0599	-0.3951	0.9373	1.05	1.25
S4	0.8147	0.6253	0.0016	0.3726	-4.3144	0.2831	0.3102	-5.2255	-0.0014	0.2440	0.95	1.30
S5	0.6577	0.5164	-0.0054	0.3159	-5.1872	0.1561	0.2300	-5.3960	-0.0670	0.9467	0.77	0.86
T1	0.6308	0.5289	-0.0072	0.3823	-6.0845	0.1402	1.7052	-5.6049	0.0580	2.0217	0.58	0.63
T2	0.5569	0.4207	0.0023	0.2817	-5.6907	-0.4720	-0.1919	-5.3891	-0.0646	-0.2641	0.51	0.47
T3	0.4310	0.3190	0.0004	0.2151	-4.9703	-0.2319	0.0257	-5.0529	-0.0408	-0.4545	0.52	0.37
T4	0.5884	0.4500	0.0022	0.3295	7.6823	-0.8842	0.1750	8.3174	-0.7977	0.1111	0.64	0.63
T5	0.4935	0.3805	0.0128	0.2405	-7.3059	-0.9161	-0.2202	-6.5374	-0.7128	0.2641	0.93	0.76

Table S6. Computed hole and electron overlap (S), distance between centroids of hole and electron (D, Å) and dipole moment (μ) for singlet states of TPATPA-CNPPI.

State	Hole integral	Electron integral	Integral of transition density	Integral overlap of h^+- e^- (S)	Centroid of hole (Å)			Centroid of electron (Å)			D (Å)	μ (a.u)
					x	y	z	x	y	z		
S1	0.8036	0.6965	-0.0072	0.3366	-6.7279	-0.1136	0.7185	-5.6223	0.2910	2.2773	1.95	2.76
S2	0.7747	0.6226	-0.0100	0.3697	-6.9832	-0.5667	0.1526	-5.9424	-0.3077	0.0928	1.07	1.41
S3	0.7210	0.5785	-0.0075	0.3558	-6.8377	-0.6075	0.0495	-6.3903	-0.2530	1.0705	1.16	1.43
S4	0.8025	0.6372	-0.0000	0.2908	-3.7352	0.5577	-0.0734	-5.3759	0.0903	1.1482	2.09	2.85
S5	0.7094	0.5599	-0.0057	0.3273	-4.7952	0.1469	-0.0208	-5.1802	0.0816	0.9439	1.04	1.24
T1	0.6614	0.5537	-0.0052	0.3912	-5.5678	0.1762	1.5464	-5.6126	0.2573	2.1025	0.56	0.64
T2	0.5648	0.4328	-0.0025	0.2770	-7.1792	-1.2476	-0.7367	-5.9410	-0.5426	-0.4958	1.44	1.36
T3	0.4205	0.3070	0.0091	0.2023	-3.1191	0.3114	-0.1874	-3.6461	0.4152	-0.6966	0.74	0.50
T4	0.6193	0.4683	-0.0017	0.3452	7.6988	-1.0051	0.1142	8.1397	-0.8233	0.1241	0.47	0.49
T5	0.5022	0.3909	-0.0098	0.2648	-6.7837	-0.8288	-0.3282	-6.4099	-0.8548	-0.1025	0.43	0.36

Table S7. Computed RMSD of electron and hole, H index and t index for singlet states of TPATPA-PPI.

State	RMSD (Electron)				RMSD (Hole)				H index				t index			
	x	y	z	total	x	y	z	total	x	y	z	Total	x	y	z	Total
S1	2.113	1.178	1.818	3.026	2.434	1.347	1.657	3.238	2.274	1.262	1.737	3.128	-0.879	-1.169	-0.750	1.643
S2	2.704	1.386	1.670	3.467	2.485	1.597	1.686	3.401	2.594	1.492	1.678	3.431	-1.237	-1.246	-1.277	2.171
S3	3.731	1.880	2.090	4.671	2.567	1.586	1.740	3.483	3.149	1.733	1.915	4.073	-2.202	-1.689	-1.449	3.131
S4	2.439	1.285	1.863	3.327	2.910	1.529	1.950	3.822	2.675	1.407	1.906	3.573	-1.763	-1.123	-1.840	2.785
S5	2.930	1.411	2.063	3.851	3.355	1.652	1.799	4.150	3.143	1.531	1.931	3.993	-2.934	-1.308	-1.214	3.434
T1	2.070	1.170	1.874	3.027	2.360	1.154	1.699	3.128	2.215	1.162	1.786	3.074	-1.735	-1.080	-1.470	2.517
T2	3.097	1.497	1.436	3.728	3.284	1.771	1.618	4.067	3.191	1.634	1.527	3.897	-2.889	-1.227	-1.455	3.460
T3	3.251	1.683	1.337	3.897	3.838	1.739	1.806	3.545	1.711	1.572	4.238	-3.462	-1.520	-1.091	3.935	4.197
T4	2.510	1.879	0.836	3.245	3.687	1.905	0.904	4.248	3.099	1.892	0.870	3.733	-2.463	-1.806	-0.806	3.159
T5	3.299	1.796	1.939	4.227	2.741	1.683	1.546	3.569	3.020	1.739	1.743	3.896	-2.251	-1.536	-1.258	3.002

Table S8. Computed RMSD of electron and hole, H index and t index for singlet states of TPATPA-CNPPI.

State	RMSD (Electron)				RMSD (Hole)				H index				t index			
	x	y	z	total	x	y	z	total	x	y	z	Total	x	y	z	Total
S1	1.850	1.076	1.864	2.838	2.646	1.434	1.745	3.479	2.248	1.255	1.805	3.144	-1.142	-0.851	-0.246	1.445
S2	3.019	1.427	1.837	3.811	2.755	1.645	1.728	3.644	2.887	1.536	1.782	3.724	-1.846	-1.277	-1.723	2.830
S3	2.547	1.685	2.179	3.752	2.561	1.660	1.783	3.534	2.554	1.673	1.981	3.639	-2.106	-1.318	-0.960	2.664
S4	2.260	1.208	2.237	3.402	2.664	1.351	1.860	3.519	2.462	1.280	2.049	3.449	-0.821	-0.812	-0.827	1.421
S5	2.637	1.254	2.215	3.665	3.485	1.692	1.827	4.283	3.061	1.473	2.021	3.953	-2.676	-1.408	-1.056	3.203
T1	1.784	1.080	1.979	2.875	2.344	1.205	1.871	3.232	2.064	1.143	1.925	3.045	-2.019	-1.062	-1.369	2.660
T2	3.270	1.552	1.499	3.918	2.540	0.947	1.691	1.350	3.337	2.905	1.622	3.619	-1.667	-0.917	-1.184	2.240
T3	3.505	1.684	1.352	4.117	3.719	1.593	1.850	4.449	3.612	1.639	1.601	4.277	-3.085	-1.535	-1.092	3.615
T4	3.058	1.845	0.889	3.282	3.103	3.680	3.548	1.937	0.918	4.145	3.303	3.912	-2.862	-1.709	-0.894	3.451
T5	2.905	2.072	2.031	4.106	3.318	1.722	1.645	4.084	3.111	1.897	1.838	4.242	-2.262	-2.492	-1.266	3.596

Table S9. Transferred charges (q_{CT}), barycentres of electron density loss (R_+) /gain (R-), distance between two barycenters (D_{CT}), dipole moment of CT (μ_{CT}), RMSD of +ve/-ve parts, CT indices (H & t) and overlap integral of C+/C- of TPATPA-PPI and TPATPA-CNPPI.

Emissive materials	q_{CT} $\lvert e^{-1} \rvert$	R_+ (Å)			R- (Å)			D_{CT} (Å)	μ_{CT} (D)	RMSD of +ve parts	RMSD of -ve parts	H / t indices (Å)	overlap integral of C+/ C-
TPATPA-PPI	19.216 - 21.012	1.930	1.447	-1.592	10.256	0.685	0.357	8.585	28.626	15.501	10.869	6.939/2.111	0.4051
TPATPA-CNPPI	25.716 - 27.646	-2.220	0.481	0.039	-2.318	0.202	0.054	0.296	36.529	14.137	13.779	7.386/7.177	0.9988

Table S10. Summary of device efficiencies and current state-of-the-art literature data for blue OLEDs that possess AIE-type emitters.

Emitter	V_{on}[V]	CE (cd/A)	EQE (%)	PE (lm/W)	EL (nm)	Ref.
TPATPA-PPI	**2.8**	**13.43**	**5.32**	**11.03**	**471**	**This work**
TPATPA-CNPPI	**2.6**	**19.58**	**8.96**	**17.82**	**457**	**This work**
NSPI-DVP	2.7	5.61	5.09	4.99	439	15
CNSPI-DVP	2.6	5.03	5.23	4.72	427	15
2TriPE-BPI	2.8	4.87	3.74	5.21	462	16
2TriPE-BPI-MCN	3.8	4.72	4.60	3.17	452	16
CNNPI	3.2	1.49	2.28	1.23	432	17
2TriPE-CNNPI	3.0	3.70	2.75	2.98	456	17
2CzPh-CNNPI	3.0	6.65	5.09	5.66	454	17
TPE-NPPB	3.0	4.32	3.2	4.01	444	18
TPE-APPB	3.0	5.28	5.3	4.92	428	18
TPEPPI	2.9	4.25	2.36	3.35	467	19
3a	3.8	-	3.9	9.00	480	20
3d	3.8	-	4.0	9.8	480	20
3a	-	11.1	5.6	-	-	21
3b	-	9.4	2.3	-	-	21
3c	-	9.4	5.0	-	-	21
TPE01-PPI	2.7	3.90	3.75	4.17	512	22
TPE04-PPI	2.7	4.22	4.07	4.51	508	22
TPE06-PPI	2.7	4.33	3.87	4.65	510	22
A1	3.67	2.84	3.62	3.02	434	23
A2	3.20	2.64	3.11	2.61	434	23
B1	4.12	3.12	3.99	3.15	440	23
B2	3.36	4.24	4.66	3.67	440	23
A	3.9	1.83	2.30	1.48	-	24
B	3.3	4.13	3.69	2.89	-	24
C	3.7	3.52	4.56	2.84	-	24
D	3.8	3.84	4.84	3.02	-	24
E	3.7	4.40	5.52	3.73	-	24
12	3.2	4.9	4.0	4.4	-	25
13	3.9	2.1	1.9	1.7	-	26
14	4.0	1.51	1.12	-	-	27
15	3.0	5.21	3.89	5.06	-	28
16	3.4	3.95	3.98	4.51	-	29
1	-	-	2.8	-	490	30
2	-	-	4.0	-	476	30
m TPE- m TPE	3.9	2.1	1.9	1.7	452	31
m TPE- p TPE	4.1	2.8	1.9	2.0	459	31
o TPE- m TPE	3.7	1.8	1.4	1.4	435	31
o TPE- p TPE	3.9	2.2	1.7	1.8	454	31
mTPE-2mTPE	4.7	1.88	1.30	1.36	449	32
pTPE-2mTPE	3.7	4.03	2.17	2.79	471	32
mTPE-2pTPE	3.5	3.67	2.09	2.90	461	32
2,5-mBTPE-TP	4.7	3.40	1.96	1.90	440	33
Py-4 methyl TPE	4.0	5.14	2.5	3.05	472	34
Py-4mTPE	3.5	4.02	2.5	3.08	436	34
I	6.6	3.1	3.1	1.5	454	35
II	6.2	4.1	4.1	2.1	454	35
III	6.7	5.3	5.3	2.8	456	35
IV	9.3	13.1	4.9	7.5	556	35
Si-p-TPE	3.5	7.40	2.92	5.57	512	36
Si-tPE	3.0	8.04	3.38	6.17	488	36
Si-mTPE	3.7	1.39	1.21	1.18	432	36
PhQ-CVz	3.1	5.82	4.48	5.50	462	37
M-tDABNA	2.7	5.7	8.6	4.0	461	38
BCz-BFPz	3.9	2.0	4.34	-	436	39
C-A-C	3.7	-	3.24	-	424	40
P2	4.25	1.3	3.9	-	401	41
Cz-Oxa-BPh	3.3	1.4	4.0	1.3	423	42
TBBA	3.2	2.52	3.2	2.73	440	43

References

[1] J. Jayabharathi, S. Panimozhi, V. Thanikachalam, *Sci Rep.* 2020, **10**, 5114.

[2] (a) M. J. Frisch, G. W. Trucks, H. B. Schlegel, G. E. Scuseria, M. A. Robb, J. R. Cheeseman, G. Scalmani, V. Barone, B. Mennucci, G. A. Petersson, H. Nakatsuji, M. Caricato, X. Li, H. P. Hratchian, A. F. Izmaylov, J. Bloino, G. Zheng, J. L. Sonnenberg, M. Hada, M. Ehara, K. Toyota, R. Fukuda, J. Hasegawa, M. Ishida, T. Nakajima, Y. Honda, O. Kitao, H. Nakai, T. Vreven, J. A. Montgomery, Jr., J. E. Peralta, F. Ogliaro, M. Bearpark, J. J. Heyd, E. Brothers, K. N. Kudin, V. N. Staroverov, R. Kobayashi, J. Normand, K. Raghavachari, A. Rendell, J. C. Burant, S. S. Iyengar, J. Tomasi, M. Cossi, N. Rega, J. M. Millam, M. Klene, J. E. Knox, J. B. Cross, V. Bakken, C. Adamo, J. Jaramillo, R. Gomperts, R. E. Stratmann, O. Yazyev, A. J. Austin, R. Cammi, C. Pomelli, J. W. Ochterski, R. L. Martin, K. Morokuma, V. G. Zakrzewski, G. A. Voth, P. Salvador, J. J. Dannenberg, S. Dapprich, A. D. Daniels, O. Farkas, J. B. Foresman, J. V. Ortiz, J. Cioslowski and D. J. Fox, Gaussian, Inc., Wallingford CT (Revision A.02), *Gaussian, Inc., Wallingford, CT.* 2009. (b) T. Lu, F. Chen, *J. Comput. Chem.* 2012, **33**, 580.

[3] R. L. Martin, *J. Chem. Phys.* 2003, **118,** 4775.

[4] T. Le Bahers, C. Adamo, I. Ciofini, *J. Chem. Theory Comput.* 2011, **7**, 2498.

[5] S. Tretiak, S. Mukamel*, Chem. Rev.* 2002,**102**, 3171.

[6] J. Jayabharathi, R. Ramya, V. Thanikachalam, P. Jeeva, E. Sarojpurani, *RSC Adv*. 2019, **9**, 2948.

[7] H. Liu, Q. Bai, L. Ya, H. Zhan, H. Xu, S. Zhang, W. Li, Y. Gao, J. Li, P. Lu, H. Wang, B. Yang, Y. Ma, *Chem. Sci.* 2015, **6**, 3797.

[8] Z. Wang, Y. Feng, H. Li, Z. Gao, X. Zhang, P. Lu, P. Chen, Y. Mab, S. Liu, *Phys. Chem. Chem. Phys.* 2014, **16**, 10837.

[9] Y. F. Chang, H. F. Meng, G. L. Fan, K. T. Wong, H. W. Zan, H. W. Lin, H. L. Huang, S. F. Horn, *Org. Electron.* 2016, **29**, 99.

[10] Y. Zhang, T. Wai, N. F. Lua, Q. X. Tong, S. L. Lai, M. Y. Chan, H. L. Kwong, C. S. Lee, *Dyes. Pigm.* 2013, **98,** 190.

[11] G. Li, J. Zhao, D. Zhang, J. Zhu, Z. Shi, S. Tao, Feng Lu, Q. Tong, *New J. Chem.* 2017, **41**, 5191.

[12] S. Liu, F. He, H. Wang, H. Xu, C. Wang, F. Li, Y. Ma, *J. Mater. Chem.* 2008, **18**, 4802.

[13] S. Kim, B. Sanyoto, W. T. Park, S. Kim, S. Mandal, J. C. Lim, Y. Y. Noh, J. H. Kim, *Adv. Mater.* 2016, **28,** 10149.

[14] X. L. Li, X. Ouyang, D. Chen, X. Cai, M. Liu, Z. Ge, Y. Cao, S. J. Su, *Nanotechnol.* 2016, **27**, 124001.

[15] J. Jayabharathi, S. Sivaraj, V. Thanikachalam, J. Anudeebhana, *Adv. Mater.* 2021, **2**, 6388.

[16] H. Zhang, A. Li, G. Li, B. Li, Z. Wang, S. Xu, W. Xu, B. Z. Tang, *Adv. Optical Mater*. 2020, **14**, 1902195.

[17] H. Zhang, B. Zhang, Y. Zhang, Z. Xu, H. Wu, P. A. Yin, Z. Wang, Z. Zhao, D. Ma, B. Z. Tang, *Adv. Funct. Mater*. 2020, **30**, 2002323.

[18] J. Jayabharathi, S. Thilagavathy, V. Thanikachalam, *Mater. Adv*. 2021, **2**, 5160.

[19] J. Shi, L. Xu, X. Lv, Q. Ding, W. Li, Q. Sun, S. Xue, W. Yang, *Dyes Pigm.* 2019, **161**, 97.

[20] T. Jadhav, J. M. Choi, B. Dhokale, S. M. Mobin, J. Y. Lee, R. Misra, *J. Phys. Chem. C* 2016, **120**, 18487.

[21] T. Jadhav, J. M. Choi, J. Y. Lee, B. Dhokale, R. Misra, *Org. Electron*. 2016, **37**, 448.

[22] Z. Qiu, Z. Yang, W. C. Chen, L. Xing, S. Hu, S. Ji, Q. Yang, N. Cai, X. Ouyang, Y. Huo, *J. Mat. Chem. C* 2020, **8**, 4139.

[23] A. Islam, Q. Wang, L. Zhang, T. Lei, L. Hong, R. Yang, Z. Liu, R. Peng, L. S. Liao, Z. Ge, *Dyes Pigm*. 2017, **17**, 30335.

[24] C. Li, J. Wei, J. Han, Z. Li, X. Song, Z. Zhang, J. Zhang, Y. Wang, *J. Mat. chem., C* 2016, **4**, 10120.

[25] W. Qin, Z. Y. Yang, Y. B. Jiang, J. W. Y. Lam, G. D. Liang, H. S. Kwok, B. Z. Tang, *Chem. Mater*. 2015, **27**, 3892.

[26] J. Huang, N. Sun, Y. Dong, R. Tang, P. Lu, P. Cai, Q. Li, D. Ma, J. Qin, Z. Li, *Adv. Funct. Mater.* 2013, **23**, 2329.

[27] X. Tang, L. Yao, H. Liu, F. Shen, S. Zhang, H. Zhang, P. Lu, Y. Ma, *Chem. Eur. J*. 2014, **20**, 7589.

[28] X. Zhan, Z. Wu, Y. Lin, Y. Xie, Q. Peng, Q. Li, D. Ma, Z. Li, *Chem. Sci*. 2016, **7**, 4355.

[29] X. Zhan, N. Sun, Z. Wu, J. Tu, L. Yuan, X. Tang, Y. J. Xie, Q. Peng, Y. Dong, Q. Li, D. Ma, Z. Li, *Chem. Mater*. 2015, **27**, 1847.

[30] A. Ekbote, S. H. Han, T. Jadhav, S. M. Mobin, J. Y. Lee, R. Misra, *J. Mater. Chem. C* 2018, **6**, 2077.

[31] J. Huang, N. Sun, Y. Dong, R. Tang, P. Lu, P. Cai, Q. Li, D. Ma, J. Qin, Z. Li, *Adv. Funct. Mater*. 2013, **23**, 2329.

[32] J. Huang, N. Sun, J. Wang, R. Tang, X. Li, J. Dong, Q. Li, D. Ma, Z. Li, *Isr. J. Chem*. 2014, **54,** 931.

[33] Z. Ruan, L. Li, C. Wang, Y. Xie, Q. Hu, Q. Peng, S. Ye, Q. Li, Z. Li, *small.* 2016, **21**, 6623.

[34] J. Yang, J. Huang, N. Sun, Q. Peng, Q. Li, D. Ma, Z. Li, *Chem. Eur. J*. 2015, **21**, 6862.

[35] P. I. Shih, C. Y. Chuang, C. H. Chien, E. W. G. Diau, C. F. Shu, *Adv. Funct. Mater*. 2007, **17**, 3141.

[36] J. Yang, N. Sun, J. Huang, Q. Li, Q. Peng, X. Tang, Y. Dong, D. Ma, Z. Li, *J. Mat. Chem., C* 2015, **3**, 2624.

[37] S. J. Lee, J. S. Park, K. J. Yoon, Y. I. Kim, S. H. Jin, S. K. Kang, Y. S. Gal, S. Kang, J. Y. Lee, J. W. Kang, S. H. Lee, H. D. Park, J. J. Kim, *Adv. Funct. Mater*. 2008, **18**, 3922.

[38] H. Lim, S. J. Woo, Y. H. Ha, Y. H. Kim, J. J. Kim, *Adv. Mat*. 2022, **34**, 2100161.

[39] C. C. Huang, M. M. Xue, F. P. Wu, Y. Yuan, L. S. Liao, M. K. Fung, *Molecules*. 2019, **24**, 353.

[40] A. Pachariyangkun, P. Wongkaew, T. Sudyoadsuk, S. Namuangruk, V. Promarak, *Dyes and Pigments*, 2021, **186**, 109065.

[41] J. Santos, J. H. Cook, H. A. Al-Attar, A. P. Monkman, M. R. Bryce, *J. Mater. Chem. C*, 2015, **3**, 2479.

[42] Y. Tan, Z. Wang, C. Wei, Z. Liu, Z. Bian, C. Huang, *Org. Electron.* 2019**, 69**, 77.

[43] Z. Li, G. Gan, Z. Ling, K. Guo, C. Si, X. Lv, H. Wang, B. Wei, Y. Hao, *Org. Electron.* 2019, **66,** 24.